Atmospheric environment shapes surface reactivity of Fe(0)-doped lunar dust simulant: Potential toxicological implications

Journal of Hazardous Materials 492 (2025) 138096

Contents lists available at ScienceDirect

Journal of Hazardous Materials

journal homepage: www.elsevier.com/locate/jhazmat

Atmospheric environment shapes surface reactivity of Fe(0)-doped lunar dust simulant: Potential toxicological implications

Cristina Pavan [a,b,c], Piero Bianco [a,b], Olimpia Tammaro [d], Micaela Castellino [d], Antonello Marocco [e], Jasmine Rita Petriglieri [b,f], Maura Tomatis [b,g], Michele Pansini [e], Serena Esposito [d,*], Francesco Turci [a,b,**]

[a] Department of Chemistry, University of Turin, via P. Giuria 7, Torino 10125, Italy
[b] "G. Scansetti" Interdepartmental Centre for Studies on Asbestos and Other Toxic Particulates, University of Turin, via P. Giuria 7, Torino 10125, Italy
[c] Louvain Centre for Toxicology and Applied Pharmacology (LTAP), Université catholique de Louvain, Brussels 1200, Belgium
[d] Department of Applied Science and Technology and INSTM Unit of Torino, Politecnico di Torino, Corso Duca degli Abruzzi 24, Torino 10129, Italy
[e] Department of Civil and Mechanical Engineering and INSTM Research Unit, Università degli Studi di Cassino e del Lazio Meridionale, Via G. Di Biasio 43, Cassino, FR 03043, Italy
[f] Department of Earth Sciences, University of Turin, Turin 10125, Italy
[g] Department of Veterinary Sciences, University of Turin, Largo Braccini, 2, Grugliasco, TO, Italy

HIGHLIGHTS

- Simulant Moon Agglutinate (SMA) with nanophase iron (np-Fe0) to simulate lunar dust for toxicity studies.
- A non-oxidative ball milling set-up was used to expose non-oxidized np-Fe^0 at particle surface.
- np-Fe^0 reduces molecular oxygen and promotes the oxidative activity of SMA.
- The oxidative activity of SMA decreases over time when exposed to a life-supporting atmosphere (oxidative ageing).
- The mechanism of toxicity of SMA is not related to cell membrane damage.

GRAPHICAL ABSTRACT

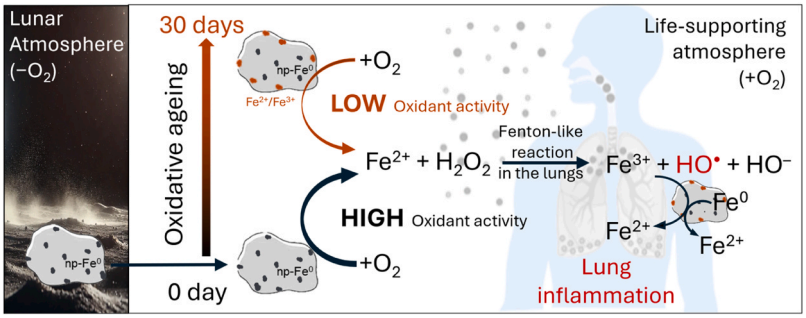

ARTICLE INFO

Keywords:
Lunar dust simulant
Nanophase iron
Oxidative stress
Regolith
Toxicity
Zero-valent iron

ABSTRACT

The toxicity of lunar dust (LD), anecdotally reported by Apollo astronauts, raises concerns for future missions involving prolonged human presence on the Moon. LD toxicity is thought to involve oxidative stress driven by nanophase metallic iron (np-Fe^0), a peculiar feature of LD. In life-supporting lunar habitat, np-Fe^0 embedded in the amorphous phases of LD may react with O_2 prior to accessing the lung, complicating toxicity assessments. Due to limited availability of real LD samples, toxicological evaluations rely on lunar dust simulants (LDS). A novel Simulant Moon Agglutinate (SMA), composed of a glassy matrix with np-Fe^0, was produced and ball milled in an inert atmosphere to expose non-oxidized Fe^0 surface centers and to obtain a dust with respirable particle size. Physicochemical properties, oxidative activity, and iron release in simulated body fluids were assessed on selected SMA samples. SMA were aged in air, and the kinetics of free radical generation revealed a strong redox

* Corresponding author.
** Corresponding author at: Department of Chemistry, University of Turin, via P. Giuria 7, Torino 10125, Italy.
E-mail addresses: serena_esposito@polito.it (S. Esposito), francesco.turci@unito.it (F. Turci).

https://doi.org/10.1016/j.jhazmat.2025.138096
Received 9 January 2025; Received in revised form 5 March 2025; Accepted 27 March 2025
Available online 10 April 2025

activity that decreased with aging. After an oxidative ageing of 1 month, SMA was still active in generating free radicals, to a higher extent that other LD simulants like JSC-1A-vf, highlighting the key role of np-Fe^0 in eliciting LD peculiar reactivity. In vitro tests showed that SMA caused no cell membrane damage, suggesting that LD toxicity mechanisms might involve free radicals and may differ from terrestrial toxic dust, such as quartz.

1. Introduction

A new era of lunar exploration is expected in the next years. Human bases on the Moon's surface are envisaged by many space agencies, including the USA National Aeronautics and Space Administration (NASA) with the Artemis program [1] and the China National Space Administration (CNSA) with the Chang'e program [2]. Additionally, EU, India, Japan, Russia, South Korea, the United Arab Emirates are planning missions to find and exploit *in situ* resources (In-Situ Resource Utilization, ISRU), including the use of lunar regolith for construction, oxygen extraction, and food production [3,4]. Despite multiple successful Apollo missions that saw astronauts land on and return from the Moon, ensuring astronauts' health remains a major challenge for ongoing lunar exploration programs. One key issue involves the impact of lunar dust (LD) on human health [5–7].

The lunar soil is covered by a dusty layer of regolith with particle size ranging from 30 nm to 20 μm, over 95 % of which is smaller than 2 μm [8]. Despite the similarity with terrestrial rocks, the LD exhibits some chemical peculiarities due to the environment in which it is formed. The lunar surface is exposed to constant micro-meteorite bombardment, for which impact temperatures may be as high as 2000 °C. The impact-melt-vapor deposition process in the lunar reducing atmosphere generates amorphous rims and metallic iron nano-agglomerates, i.e., nanophase iron (np-Fe^0), embedded in a glassy silicate matrix, a characteristic that is absent in terrestrial minerals [9,10]. On the surface of lunar soil particles, np-Fe^0 is the dominant crystalline phase within rims formed on individual grains of amorphous glass or agglutinates [10]. The concentration of np-Fe^0 in returned lunar soil samples has been determined by magnetic methods and Mössbauer spectroscopy, revealing metallic iron contents of about 0.5–1 wt% [11].

During their permanence on the Moon, astronauts face significant exposure to LD, especially when these fine particles are carried into the lunar module upon their return from extravehicular activities (EVA) [5,12]. The astronauts of the Apollo missions described respiratory and dermal effects of the LD, including cough, sore throat, allergic reaction, nostrils irritation, and burning eyes [12–14]. Apollo's astronauts were exposed to LD for a very short time, while future missions envisage human presence for much longer periods, lasting up to a few months. To ensure astronauts safety, those future missions must take into account higher level of exposure and long-term toxicity effects of LD [15].

The toxicity of LD has been investigated in *in vitro* and *in vivo* studies. Lung toxic effects, including increase of inflammatory biomarkers and impairment of alveolar capillary barrier, have been identified in rats treated with LD [16,17]. Alveolar macrophages and lung epithelial cells showed a decrease in cell viability, DNA damage, and release of pro-inflammatory factors after LD exposure [18–20]. Studies have shown the intrinsic ability of LD to boost cellular oxidative stress by generating high levels of reactive oxygen species (ROS), including the highly oxidant hydroxyl radicals ($^{\bullet}OH$), through Fenton-like mechanism that may involve np-Fe^0 [21–25]. ROS are known to be extremely damaging to cellular components, with $^{\bullet}OH$ being particularly harmful due to its strong oxidation potential (2.4 V for the $^{\bullet}OH$ /H_2O redox couple) and its ability to oxidize a wide range of organic molecules [26]. Notably, $^{\bullet}OH$ plays a crucial role in initiating lipid peroxidation in biological systems and is capable of oxidizing DNA, proteins and phospholipids [27].

Because of the limited amount of real LD recovered from Apollo, Luna, and Chang'e-5 missions, many LD simulants (LDS) have been developed in the laboratory [28–30]. These materials seek to mimic the main physico-chemical characteristics of real LD, such as size and composition [6,31]. However, only a few simulants have been used for toxicological studies, as replicating the precise chemistry and reactivity of real LD remains challenging [22]. A major limitation of all current lunar simulants, including the NASA's Johnson Space Center-1A (JSC-1A) simulant that has been largely used in toxicity studies [19,32], is the lack of np-Fe^0 inclusions and glassy agglutinates [33,34]. Only a very few lab-scale successful attempts have been made to obtain reduced iron clusters in simulants, by chemical reduction of well-known LDS [22] or from precursors [34]. Thus, developing high fidelity LDS remains crucial for accurately assessing the potential health hazard of LD and ensure safe human exploration of the Moon.

In this study, we fine-tuned the surface properties of a newly developed LDS rich in np-Fe^0 to investigate its surface reactivity and biochemical processes related to the occurrence of np-Fe^0. Specifically, we explored potential oxidative mechanisms underlying the toxic effects of LD, considering both its initial, non-oxidative environment (Moon-like conditions) and the alterations induced by oxidative ageing upon exposure to an oxygen-rich life-supporting atmosphere. It is largely held that the reductive molecular environment in which LD is generated may define its surface reactivity and we hypothesized here that the exposure to an oxygen-rich atmosphere may affect the speciation of surface iron and eventually modulate LD oxidative potential, which in turn may define LD toxicity.

The molecular mechanisms leading to oxidative stress and $^{\bullet}OH$ formation induced by np-Fe^0 remain poorly understood in the literature on lunar and planetary science, the most widely cited mechanism being the Fenton reaction [22], in which superficial ferrous iron (Fe^{2+}) reacts with hydrogen peroxide (H_2O_2) produced in lysosome of phagocyting macrophage cells, forming $^{\bullet}OH$:

$$Fe^{2+} + H_2O_2 \rightarrow Fe^{3+} + {}^{\bullet}OH + OH^- \quad (1)$$

This gap in surface reactivity studies related to np-Fe^0 role in LD toxicity arises primarily because, to the best of our knowledge, only a few studies have successfully obtained a LDS with np-Fe^0 [22], and none of them have prepared and stored the simulant under a controlled atmosphere. Because metallic iron (Fe^0) rapidly reacts with atmospheric O_2, our LDS was carefully prepared and stored in an inert non-oxidative atmosphere. Our protocol ensured that this LDS was first exposed to O_2 only at the exact moment when surface reactivity tests or oxidative ageing experiments began. This complex procedure was designed to simulate the moment when LD enters the interlock, is exposed to oxygen, and potentially reaches the human respiratory tract. To achieve this, we designed an experiment to systematically study the effect of oxidative ageing (up to one month) on the surface reactivity of the simulant.

Drawing insights from studies on contaminant remediation where the chemistry of Fe^0 has been largely studied, Fe^0 might lead to oxidative stress and $^{\bullet}OH$ formation in aqueous systems through reactions with atmospheric O_2. These reactions could:

i. directly involve Fe^0, generating Fenton reactants [35,36]:

$$Fe^0 + O_2 + 2H^+ \rightarrow Fe^{2+} + \quad H_2O_2 \quad (2)$$

ii. indirectly involve Fe^0 corrosion and Fe^0 corrosion products [37–40]:

$$Fe^0 + 2H^+ \rightarrow Fe^{2+} + \quad H_2 \quad (3)$$

Fe^0 corrosion in the near neutral pH yields a solid multi-layered oxide shell composed of corrosion products (i.e., FeO, FeOOH, Fe_2O_3, Fe_3O_4) at the metal surface. These reactions generate ferrous compounds that can react with atmospheric O_2 leading to ROS, including superoxide species ($O_2^{-\bullet}$), in turn forming Fenton reactants and $^\bullet$OH [41]:

$$Fe^{2+} + O_2 \rightarrow Fe^{3+} + \quad O_2^{-\bullet} \tag{4}$$

$$Fe^{2+} + O_2^{-\bullet} + 2H^+ \rightarrow \quad Fe^{2+} + H_2O_2 \tag{5}$$

The role of O_2 and the amount and speciation of bioavailable iron were here evaluated to clarify the mechanism of $^\bullet$OH generation from LDS that were developed from two zeolite types (*i.e.*, type A and type X), with different iron content— higher in type A and lower in type X [34]. This novel LDS, identified as Simulant Moon Agglutinate (SMA), simulated the glassy agglutinates containing np-Fe^0, which were detected on Apollo return samples and recently confirmed on the Chang'e-5 samples from the lunar south pole [10,34]. Quantitative phase analysis (QPA) results, as obtained by the Rietveld method, revealed np-Fe^0 contents of 2.6 wt% (SMA A) and 1.6 wt% (SMA X) [34]. These values fall within the range of reduced iron measured in lunar dust samples returned from Apollo missions [11]. Non-oxidized Fe^0 surface centers were obtained by milling SMA dust in an inert, non-oxidative atmosphere, while reducing particle size to the respirable range. Surface sensitive measures and tests, including terephthalate and radical assays, surface iron leaching in simulated body fluids, and particle-induced membrane damage, were used to probe the effect of oxidizing atmosphere on np-Fe^0 rich SMA.

2. Materials and methods

2.1. Simulant moon agglutinates

The pristine SMA A (**Ap**) was prepared from reagent grade zeolite 4 A (framework type LTA, $Na_{12}Al_{12}Si_{12}O_{48}{\cdot}27H_2O$, Carlo Erba), which was contacted with a 0.1 M [Fe^{2+}] aqueous solution prepared by dissolving $FeSO_4{\cdot}7H_2O$ (Carlo Erba) in doubly distilled water (DI) at a weight solid/liquid ratio of 1/100, for 2 h, at about 7 °C, under Ar bubbling to prevent Fe^{2+} oxidation to Fe^{3+} [44]. The solid was separated from the liquid by filtration, washed with DI water and again contacted with a fresh aliquot of the same 0.1 M [Fe^{2+}] aqueous solution, under the same conditions. This sequence of operations was iterated six times. Finally, the dust was dried overnight at 80 °C and then stored at *ca.* 50 % relative humidity to achieve zeolite water saturation. The pristine SMA X (**Xp**) was prepared from reagent grade zeolite 13X (framework type FAU, $Na_{86}Al_{86}Si_{106}O_{384}{\cdot}264\ H_2O$, Carlo Erba) by using the same procedure previously described for zeolite 4 A, the only difference being the number of iterations (i.e., three). The procedure has been slightly modified from that reported in a previous work [34]. The Fe content was 16.9 and 13.1 wt% for type A SMA and type X SMA, respectively, which was assessed and calculated elsewhere [34]. Variations in cation exchange capacity, cage size, and pore structure between these two Fe-exchanged zeolite samples likely explain their differing Fe content [34].

The Fe-exchanged zeolite samples were placed in Pt crucibles and heated up to 750 °C (15 °C/min heating rate) for 2 h in a Al_2O_3 cylindrical furnace (inner diameter 6.9 cm, length 91 cm) under a reducing atmosphere of H_2/Ar flow (H_2 = 2 % vol.). The samples (Ap and Xp) were cooled to room temperature (RT) in the closed furnace.

Both Ap and Xp samples were milled in a planetary mill (FRITSCH P6) using a zirconia jar (45 ml) which was loaded with 1 g of zirconia beads (5 mm) and 3 g of SMA dust. The milling process was performed in an inert atmosphere by using a MBraun LABstar glove box filled with pure 5.5 grade argon (pO_2 < 0.5 ppm, pH_2O < 0.5 ppm), following a procedure previously described [45]. Three milling cycles were performed at 350 rpm for 20 minutes each, with 2-minutes intervals between cycles. The milled dust was collected in the inert atmosphere of the glove box. A fraction of the milled sample was stored in the inert atmosphere (**Ai** and **Xi**), while a fraction was exposed to air (79–21 % mix of N_2 and O_2, respectively, and RH% = 30–40 %) for 1 minute (**Aa1** and **Xa1**), 72 hours (**Aa2** and **Xa2**) and 1 month (**Aa3** and **Xa3**).

2.2. Reference sample JSC-1A-vf

The well-known simulant JSC-1A-vf was used as reference material in the sodium terephthalate assay. This sample was kindly supplied by NASA Johnson Space Center (Houston, Texas, USA) and consisted of a fine fraction (< 20 μm) of JSC-1A, which was sourced from the Merriam Crater (Flagstaff, Arizona, USA). The mineralogical and chemical properties of JSC-1A-vf were similar to those of JSC-1A [46,47]. The composition of JSC-1A was basaltic tuff ash, containing about 50 % glassy material by weight, and closely resembling the lunar soil samples collected during the Apollo 17 mission [48]. However, JSC-1A-vf contained iron in the form of Fe^{2+} (*ca.* 76 % of the total iron) and Fe^{3+} (*ca.* 24 % of the total iron), and it did not contain np-Fe^0 [33,48].

2.3. Morphological analysis

The micromorphology of the particles was assessed by Field-Emission Scanning Electron Microscopy (FE-SEM) using a TESCAN S9000G microscope equipped with a Schottky FEG source. Dry particles were deposited on conductive stubs, covered with carbon tape, and analyzed within a magnification range of 10,000x to 200,000x and acceleration voltage of 15–20 kV. Micrographs were collected via secondary electrons (SE) and backscattered electrons (BSE).

2.4. Particle size distribution

The size distribution of particles in aqueous suspension was assessed by Flow Particle Image Analysis (FPIA) using a Sysmex FPIA-3000 instrument (detection range, 0.8–160 μm; Malvern Instruments), following a procedure previously described [49]. Briefly, particles were dispersed in ultrapure water (Milli-Q, Merck Millipore) at a concentration of 1 mg/ml. Particle dispersions were injected (*ca.* 5 ml) into the measurement cell under constant agitation at 360 rpm to avoid particle sedimentation. Images of the particles were captured using stroboscopic lighting and a charge-coupled device camera, using 20 × magnification in high power field (HPF) mode and low power field (LPF) mode. Data was processed with the Sysmex FPIA software.

2.5. Specific surface area (SSA)

The analysis of the SSA was performed by the Brunauer–Emmett–Teller (BET) method by measuring the adsorption of Kr at −196 °C with an ASAP 2020 adsorption analyzer (Micromeritics). The dust samples were degassed for 4 h at 200 °C before the analysis. The BET surface area was then calculated over the range P/P_0 = 0.05 – 0.25 (12 points).

2.6. Crystallographic structure

Crystallinity was assessed by X-Ray Powder Diffraction (XRPD) in the Bragg-Brentano configuration on a Philips X'Pert diffractometer. The measurements were conducted at RT in the 2θ range = 10° − 60° (step, 0.02° 2θ; time per step, 1 s). The crystallite size was calculated by the Scherrer formula:

$$\tau = \frac{k\,\lambda}{\beta \cos\theta} \tag{6}$$

where, τ is the mean size of the crystalline domains, k is a constant equal to 0.90, λ is the X-ray wavelength equal to 0.154 nm, β is the full width at half maximum, and θ is the half diffraction angle.

2.7. Surface elemental composition

The surface composition was assessed by X-ray Photoelectron Spectroscopy (XPS) using a Versaprobe Physical Electronics (PHI) 5000 spectrometer, equipped with a monochromatic Al K-alpha X-ray source (1486.6 eV). The measurements were carried out using double charge compensation, an electron gun, and a beam of Ar^+ ions to reduce surface charging effects. Survey and High Resolution (HR) spectra were acquired with different pass energies, *i.e.*, 187 eV and 23 eV, respectively. Data were analyzed using Multipak 9.0 dedicated software, by subtracting the background contribution with a Shirley function. Because this system lacks a glove box chamber, all the samples, including the ones stored in the inert atmosphere, were exposed to air before entering the analysis chamber. Thus, all samples analyzed through XPS should be considered as air exposed.

2.8. Fluorimetric determination of hydroxyl radicals by the sodium terephthalate (TA) assay

The TA assay is based on the formation of the fluorescent 2-hydroxyterephatalate (TA-OH) when the non-fluorescent TA reacts with ROS. The protocol was used in previous studies on LDS [48,50]. Briefly, SMA samples (5 mg/ml) were incubated in 10 mM TA diluted in phosphate buffer saline (10 mM PBS, Merck) at 25°C under continuous shaking. Aliquots of the suspension (2 ml) were taken after 48 h of incubation and centrifuged at 10,000 rcf for 2 min (Rotina 380 R, Hettic Instruments). The supernatant was filtered through a syringe with a filter of 0.22 µm pores (Merck Millipore). The fluorescence of the filtered solution was analyzed with a Cary Eclipse Fluorescence single-beam spectrophotometer (Varian) into a quartz cuvette using an excitation wavelength of $\lambda_{ex} = 324$ nm and an emission of $\lambda_{em} = 424$ nm. The JSC-1A-vf, which showed radical activity in the TA assay [50], was used as a positive reference material for this test. The concentration of the SMA samples and the incubation timing were selected based on a preliminary experiment with different concentrations (*i.e.*, 5, 15, and 30 mg/ml) and incubation timings (*i.e.*, 0.5, 5, 24, 48, and 96 h) of JSC-1A-vf (Appendix A, Supplementary Material, Fig. S1). Because the 5 mg/ml concentration demonstrated a linearity of the fluorescence emission, which was relatively high after 48 h incubation timing, these parameters were selected for testing SMA samples (Fig. S1). The hydroxylation of TA in the absence of SMA or JSC-1A-vf (negative control) was tested and resulted in a negligible reactivity (Fig. S1). Furthermore, a calibration curve with several concentrations of TA-OH was created to investigate the linearity interval of the reaction (Supplementary Material, Fig. S2). A 1 mM TA-OH solution was prepared in PB. Further dilutions were made from this stock solution. For concentrations above 5 µM, the fluorescence of TA-OH saturated the detector.

The SMA samples stored in the inert atmosphere (Xi and Ai) were manipulated and weighed in the argon-filled glove box to prevent any contact of the dust with air before suspension in the TA reagent. The dust was extracted from the glove box in rubber sealed glass vials that were pierced with a syringe needle containing the buffered TA solution. The samples exposed to air (Aa1–3 and Xa1–3) were manipulated under conventional lab environment.

To investigate further the mechanisms of the reactivity of SMA towards TA, the assay was carried out in oxygenated ($+O_2$) and oxygen-free ($-O_2$) solutions. The $-O_2$ test was carried out in a glove-bag filled with N_2 and all the solutions were carefully stripped for *ca.* 1 h with high-purity N_2 (5.5 grade). To avoid any possible contact with atmospheric O_2, the SMA+TA suspensions were sealed and exposed to air only after SMA was removed by centrifugation.

2.9. Fenton-like activity assessment via spin-trapping of hydroxyl radicals

The formation of hydroxyl radicals ($^{\bullet}OH$) in physiological-like solution was assessed by Electron Paramagnetic Resonance (EPR) spectroscopy coupled with the spin trapping technique by using a MiniScope 100 spectrometer (Magnettech, Germany). SMA samples (10 mg) were mixed with 625 µl of PB (10 mM, pH 7.4), 5,5-dimethyl-1-pyrroline-N-oxide (DMPO, 34 mM), and H_2O_2 (80 mM). The test investigates the Fenton-like reaction generating oxidized iron and hydroxyl radicals from reaction of hydrogen peroxide with the reduced iron provided by the dust [42]. DMPO acts as the spin trapping agent by stabilizing the $^{\bullet}OH$ in the [DMPO-OH]$^{\bullet}$ adduct. The suspension was kept on a vibrating apparatus at 37 °C. After 10, 30, and 60 min, an aliquot of the suspension (50 µl) was taken with a glass microcapillary and the EPR spectra was recorded. For samples stored in the inert atmosphere, any possible air contact was prevented by manipulating and weighing the milled SMA samples in the argon-filled glove box in sealed glass vials that were pierced with a syringe needle containing test solutions of PB, DMPO and H_2O_2. Each tested condition was repeated in at least two independent experiments. The EPR spectra (Supplementary Material, Fig.S3) were double integrated to obtain quantitative data with OriginPro 2023 Academic (OriginLab Corp.) software and the values were averaged for each tested condition.

2.10. Determination of bioavailable iron

The determination of bioavailable iron was performed according to previous studies [51]. To evaluate Fe^{2+} release, SMA samples (0.5 mg/ml) were weighed into glass vials and incubated with 0.5 mM ferrozine (10 ml). To evaluate the release of total iron (i.e., Fe^{2+} and Fe^{3+}), SMA samples (0.5 mg/ml) were incubated in a 10 ml solution containing 0.5 mM ferrozine and 0.5 mM ascorbic acid. The suspensions were incubated on an orbital shaker at 37 °C and the absorbance of the Fe^{2+}-ferrozine complex (absorption peak at 562 nm) was measured after 10 min, 30 min, 60 min, 24 h, 48 h, and 120 h, with a UV–vis spectrophotometer (Uvikon 930, Kontron).

2.11. Membranolytic activity

The membranolytic activity of SMA samples was evaluated using red blood cells (RBCs) purified from sheep blood in Alsever's solution (ThermoFisher Oxoid). The RBCs were purified by washing three times with a saline solution (Eurospital) and centrifugating at 3,200 rcf for 2 min (Rotina 420 R, Hettic Instruments). The RBCs were resuspended in Phosphate Buffer Saline (PBS, Merck) to a 5 % by volume concentration. The samples were dispersed in PBS to a final concentration of 10 mg/ml, sonicated 2 min in an ultrasound bath (Falc Instruments), and diluted to the required concentrations. A quartz sample of known membranolytic and toxic activity, i.e., Min-U-Sil 5 (US Silica Company, Berkeley Springs, WV, USA), was used as positive reference material [49,52,53]. PBS and 0.1 % Triton X-100 (Sigma-Aldrich) were used as negative and positive controls, respectively. On a 96-well plate, each well was loaded with 150 µl of particle suspensions or controls and 75 µl of the RBC suspension. The plate was incubated on an orbital shaker at 37 °C for 30 min, then centrifuged at 216 rcf for 5 min. At the end of incubation, the supernatant was transferred to a new plate and the hemoglobin released (absorption peak at 540 nm) was analyzed by an EnSight Multimode Plate Reader UV/vis spectrophotometer (PerkinElmer). The % of hemolysis was calculated according to the formula:

$$\%Hemolysis = \frac{(A_s - A_N)}{(A_P - A_N)} \quad x \quad 100 \tag{7}$$

where A_S is the absorbance of the SMA sample, A_N is the absorbance of the negative control (*i.e.*, PBS) and A_P is the absorbance of the positive control (*i.e.*, 0.1 % Triton X-100).

3. Results

3.1. Effect of milling on the physico-chemical characteristics of SMA samples

To expose np-Fe^0 centers and generate respirable dust, the pristine SMA samples (Ap and Xp) were ball milled in a planetary mill under an inert atmosphere (Ar, $pO_2 < 0.5$ ppm, $pH_2O < 0.5$ ppm), simulating the lunar atmosphere. A fraction of the milled SMA samples was stored in the inert atmosphere (Ai and Xi), while another was exposed to air (Aa and Xa) (Fig. 1 A). Both fractions were used for surface reactivity tests. However, the solid state characterization was performed on air-exposed milled SMA particles (Aa and Xa) and compared to their respective pristine, non-milled dust (Ap and Xp). This approach accounts for the fact that dust oxidative ageing affects only the uppermost atomic layers of SMA, without altering its bulk structure.

The morphological analysis carried out by FE-SEM showed that pristine SMA particles (Ap and Xp) are characterized by irregular surface structure and size, ranging from a few micrometers to some hundred nanometers (Fig. 1B). Notably, well-defined cubic structures of *ca.* 50–150 nm were identified. BSE images showed that these cubic structures appear much brighter than the rest of the sample. BSE electrons penetrate deeper into the particles and show differences in average atomic number as differences in brightness. This suggests the occurrence of np-Fe^0 as bright areas on the particle surface, a peculiar characteristic of the LDS under study [34]. After milling (Aa and Xa), particle size is reduced, and the cubes exhibit less defined surfaces.

The SSA of the particles (Fig. 1 C) ranged from *ca.* 7–8 m^2/g for Ap and Xp, and *ca.* 4–5 m^2/g for milled Aa and Xa. The reduction of the SSA of both SMA samples after milling may appear counterintuitive since milling causes a reduction in particle size, thus an increase in the SSA would be expected. However, pristine SMA samples demonstrated a residual porosity [34]. As the SSA is due to both the external surface and the surface due to porosity, the collapse of the pores during milling processes could determine a reduction of the total SSA. This effect may explain why pristine SMA shows a total larger SSA than milled SMA.

The reduction in particle size after milling was confirmed by automatic analysis of light microscopy images (FPIA analysis) of the particles suspended in water. The frequency (%) and cumulative distributions of the Circle Equivalent (CE) diameter, *i.e.*, the diameter of the circle having the same projected area of the particle image, of pristine *vs* milled SMA are reported in Fig. 2. The cumulative distributions of CE diameters showed a decrease in particle size, especially for sample X (Fig. 2B). Ap exhibited a very fine particle size distribution, the 94.8 % of particles showing diameters below the respirable size range of 3 μm [7,54], thus milling only induced a decrease in size of the larger particles (in the range 2–10 μm) (Fig. 2A). The cumulative size of Xp was larger (82.2 % particles < 3 μm), thus milling was more effective in reducing the overall particle size of type X SMA (Xa) (Fig. 2B).

The XRPD patterns of the pristine SMA samples (Ap and Xp) and the

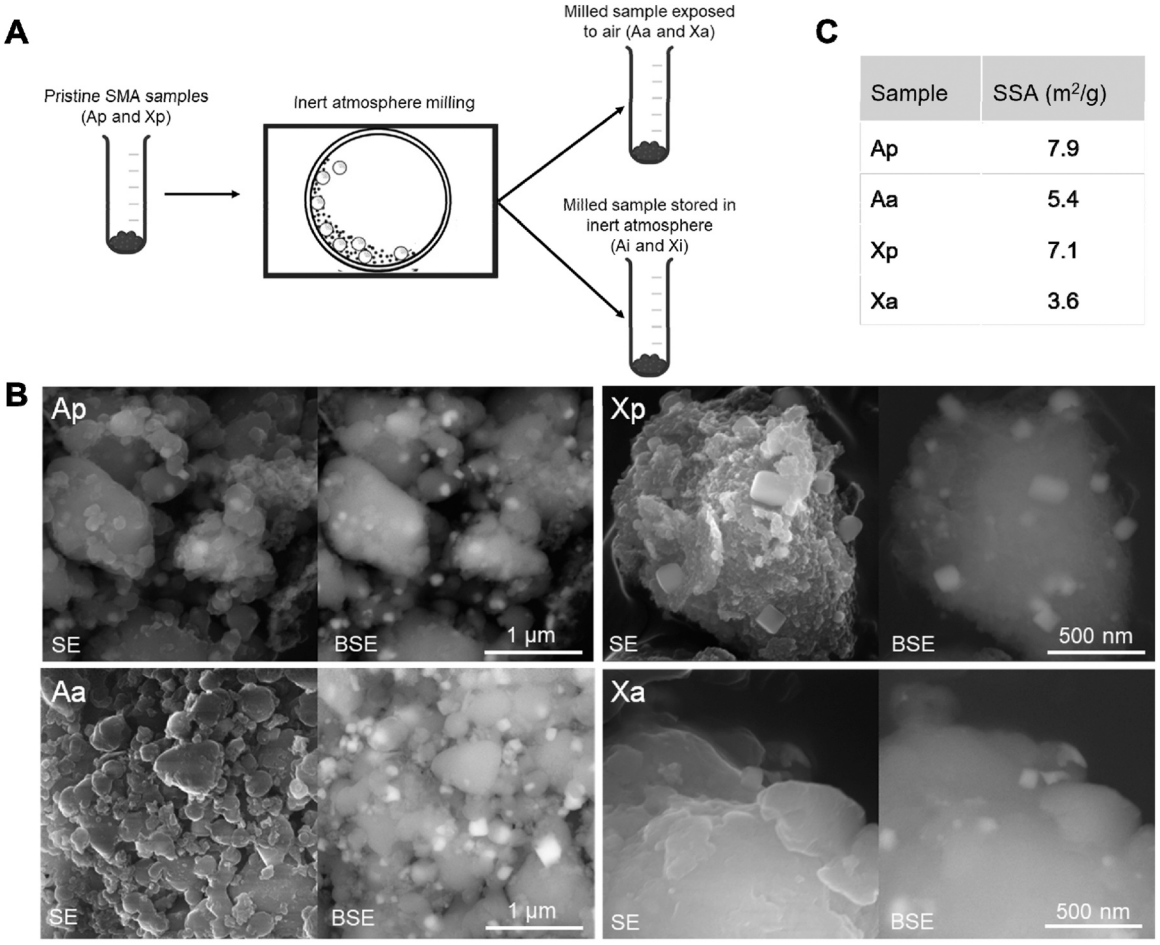

Fig. 1. (**A**) Scheme of milling and storing for type A and type X SMA samples. The pristine SMA samples (Ap and Xp) were milled in the inert atmosphere. The milled samples exposed to air (Aa and Xa) were used for assessing physico-chemical characteristics compared to the pristine particles (Ap and Xp). (**B**) FE-SEM micrographs collected via secondary electrons (SE) and backscattered electrons (BSE) of pristine (Ap and Xp) and milled (Aa and Xa) SMA. For type A samples, images were captured at a lower magnification (100k×) than for type X samples (200k×). (**C**) Specific surface area (SSA) assessed by BET analysis of the pristine (Ap and Xp) and milled (Aa and Xa) SMA particles.

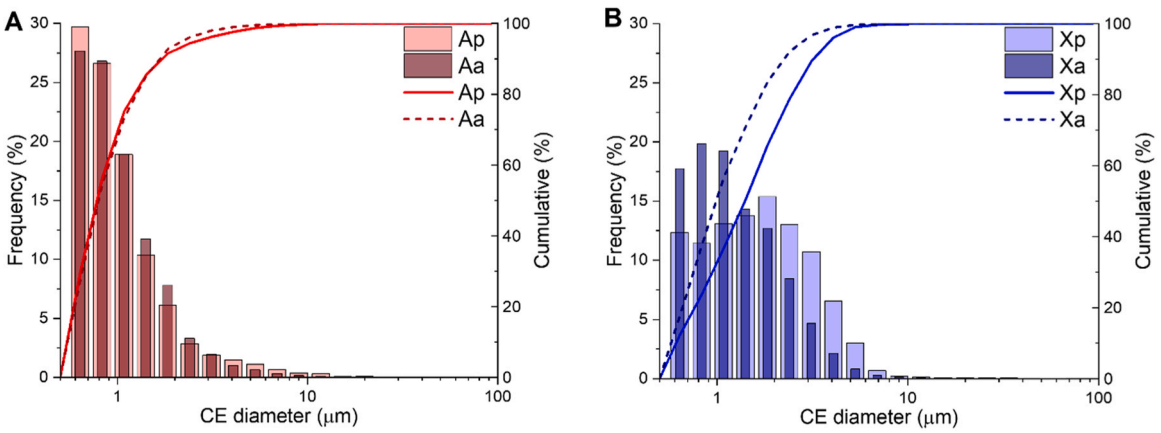

Fig. 2. Frequency (%) and cumulative distributions of the circle equivalent (CE) diameter of type A (**A**) and type X (**B**) SMA samples, before (Ap and Xp) and after milling (Aa and Xa).

milled counterparts (Aa and Xa) is reported in Fig. 3. The collapse of the zeolite framework following the reduction treatment at 750 °C led to an amorphous phase that was observed from the broad, weak signal at about 24° 2θ [55]. Only the Ap pattern showed some broad peaks referring to residual fayalite phase of the pristine zeolite (asterisks at about 35.8° 2θ and 31.6° 2θ, Fig. 3A). The single sharp peak at 44.5° 2θ, which was characteristic of all pristine and milled A and X samples, corresponds to the 110 plane of the α-Fe^0 phase (JCPD card. no. 06–0696) [34]. With both Ap and Xp, milling resulted in: i) a decrease of the intensity of the peak at about 44° 2θ due to the iron phase; ii) a broadening of the same peak, indicating a reduction in crystallite size. This observation was also supported by calculation of the crystallite size with the Scherer formula (Table 1). Thus, the milling procedure adopted led to the exposure of smaller np-Fe^0 clusters while preserving their crystallinity.

To obtain more information on the distribution of iron on the surface of SMA sample, an XPS survey was performed, and HR spectra were acquired for pristine (Ap and Xp) and milled samples exposed to air (Aa and Xa). The survey spectra (Fig. 4) showed the presence of the elements expected in the structure of the zeolite (*i.e.*, Si, Al, Na, O and Fe) and C, the latter mostly due to environmental exposure. No Zr signal was detected in the milled samples, indicating that the milling procedure in ZrO_2 jars did not introduce any sort of contamination on particle surface. Relative atomic concentrations (at%) (Table 2) were evaluated from HR spectra (not reported), to obtain values more reliable than the one calculated from survey spectra, since both pristine samples showed very low intensity peaks, especially the ones related to the Fe2p region (Supplementary Material, Fig. S4). As reported in Table 2, a clear trend in the amount of iron species available in the first (nominal) 10 nm of SMA samples is evident. Both milled samples showed a higher amount of Fe with respect to the pristine ones. In particular, pristine A and X samples showed 3.8 and 1.3 at% of Fe, respectively, while milled Aa and Xa samples showed 8.7 and 4.2 at%, respectively. This demonstrated that milling of SMA produced simulants with a surface richer in Fe than pristine SMA. Notably, type A SMA showed a larger amount of surface iron with respect to type X SMA, reflecting bulk assessments that have been formerly performed [34].

Table 1
Crystallite size obtained from elaboration of XRPD patterns. FWHM (full width at half maximum) was used to calculate the crystallite size through Scherrer equation.

Sample	Peak position (2θ)	FWHM	Crystallite size (nm)
Ap	44.5	0.158	54
Aa	44.5	0.260	33
Xp	44.5	0.165	54
Xa	44.5	0.261	33

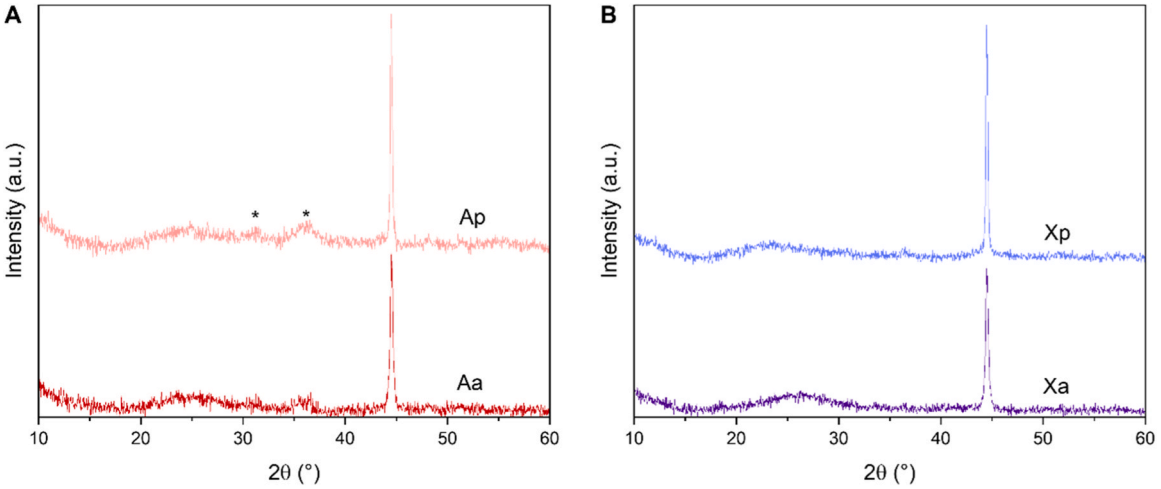

Fig. 3. XRPD diffraction patterns of type A (**A**) and type X (**B**) SMA before (Ap and Xp) and after milling (Aa and Xa).

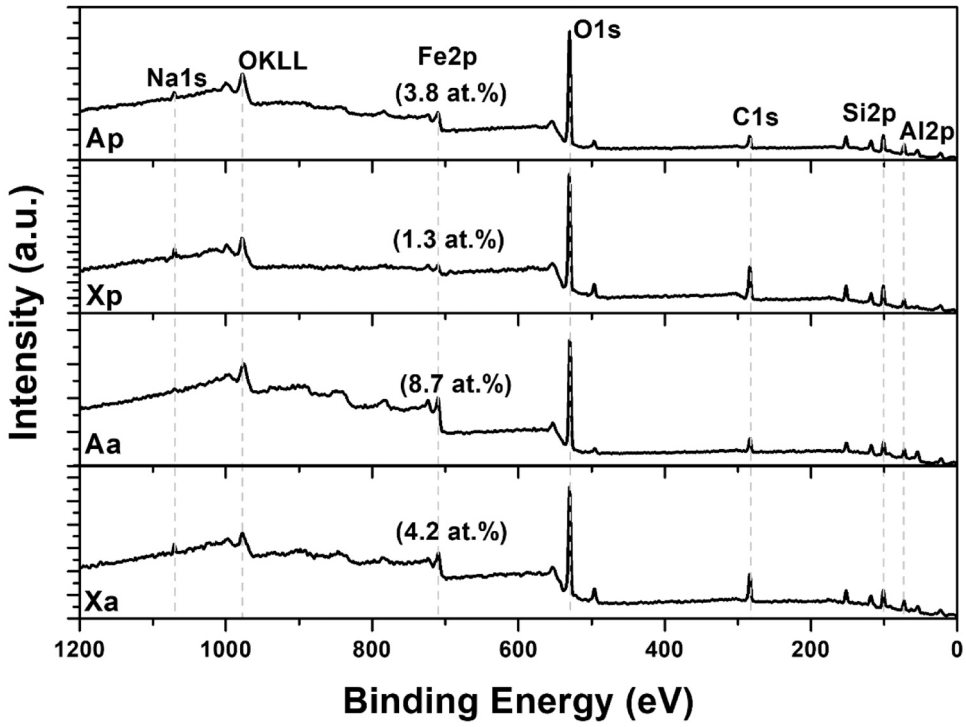

Fig. 4. XPS survey spectra of pristine (Ap and Xp) and milled (Aa and Xa) SMA. Fe2p photopeak is quantitatively integrated from HR spectra (Supplementary Material, Fig. S4) and relative atomic concentration (at%) of Fe is reported. OKLL refers to the Auger transition of oxygen electron.

Table 2
Relative atomic concentration (at%) obtained from XPS-HR spectra.

Sample	Relative atomic concentration (at%)					
	C1s	**O1s**	**Na1s**	**Fe2p**	**Si2p**	**Al2p**
Ap	15.9	53.1	1.5	3.8	14.3	11.4
Aa	16.2	53.8	1.4	8.7	10.0	9.9
Xp	31.4	44.8	2.6	1.3	12.2	7.7
Xa	26.0	48.0	1.9	4.2	11.6	8.3

3.2. The oxidant activity of milled SMA is affected by ageing in an oxidative environment

To assess the reactivity of SMA in terms of generation of reactive $^{\bullet}$OH when the dust is inhaled and encounters lung fluids and cells, SMA were contacted with sodium TA and the formation of TA-OH, which is the fluorescent product of the addition of $^{\bullet}$OH on TA [48], was determined. The experiment was designed to investigate SMA surface reactivity once the dust is transferred from the oxygen-free lunar environment (initial state) to the oxidizing life-supporting atmosphere of the interlock chamber and, eventually, to the habitat module. A scheme of the samples tested and the timing of exposure to oxidizing atmosphere is presented in Fig. 5 A. Samples milled and stored in the inert atmosphere (Ai and Xi) were exposed to conventional lab air for 1 min (Aa1 and Xa1), 72 h (Aa2 and Xa2), and 1 month (Aa3 and Xa3) before testing, to evaluate the kinetic of surface passivation and simulate oxidative ageing that may affect LD surface reactivity before inhalation. The lunar dust simulant JSC-1A-vf was used as internal reference and to optimize experimental parameters because of its well-known oxidant activity [48, 50] (Fig. S1).

The hydroxylation of TA induced by SMA samples milled in inert atmosphere (Ai and Xi) and then exposed to air for the different time points (Aa1–3 and Xa1–3) is shown in Fig. 5B. Both Ai and Xi, as well as Aa1–3 and Xa1–3, strongly induced TA hydroxylation compared to the negative control and JSC-1A-vf. Ai and Xi showed the highest oxidant activity. The activity progressively decreased with the exposure time of SMA to air. Nonetheless, after 1 month of air exposure, type A and X SMA (Aa3 and Xa3) still exhibited significantly higher oxidant activity than JSC-1A-vf. To further elucidate the molecular mechanism of TA hydroxylation by milled SMA, the test was carried out in an oxygen-deprived environment, using a N_2-filled glove bag and thoroughly purging the buffer solution with N_2. When oxygen was stripped out from the system, the reactivity of SMA Ai, Aa2, and Xa2, and to a lower extent SMA Xi, was reduced, although not completely suppressed (Fig. 5 C).

The formation of $^{\bullet}$OH and the effect of the environment on SMA oxidant activity was also evaluated in biological-relevant media, containing PB (physiological pH= 7.4), DMPO as spin trapping agent, and H_2O_2. The generation of $^{\bullet}$OH in the presence of H_2O_2 mimics reactions that might occur when particles encounter the oxidative environment of body fluids, inflamed tissue, and cellular structures, including the lysosomal fluid within alveolar macrophages and polymorphonuclear cells, which are involved in particle clearance in the lungs [56]. Hydrogen peroxide may react, via the Fenton reaction, with redox-active transition metal ions at the particle surface (e.g., Fe^{2+}) inducing the formation of $^{\bullet}$OH [50]. The EPR signal of the [DMPO-OH]$^{\bullet}$ adduct generated by SMA particles was recorded at 10, 30 and 60 min after starting the incubation with DMPO and H_2O_2 (Fig. S3). In Fig. 6, the double integration of the EPR signal for the milled SMA preserved in the inert atmosphere (Ai and Xi) and the air-exposed samples (1 min- Aa1 and Xa1, 1 month- Aa3 and Xa3) is reported. As observed in the TA assay, the SMA samples Ai and Xi showed the strongest generation of $^{\bullet}$OH radicals, especially in the first minutes of incubation, the amount of $^{\bullet}$OH gradually decreasing over 1 h. Notably, the generation of $^{\bullet}$OH induced by SMA samples drastically decreased when the particles were exposed to air for 1 min (Aa1 and Xa1). Exposing the SMA samples to air for a longer time (1 month, Aa3 and Xa3) did not further decreased the $^{\bullet}$OH generation with respect to short time exposure (1 min, Aa1 and Xa1), indicating that surface passivation and reactivity is blunted almost instantly after contact with the oxidant environment. It should be considered that, despite the great decrease, the Fenton-like $^{\bullet}$OH radical generation induced by SMA samples exposed to air was intense and

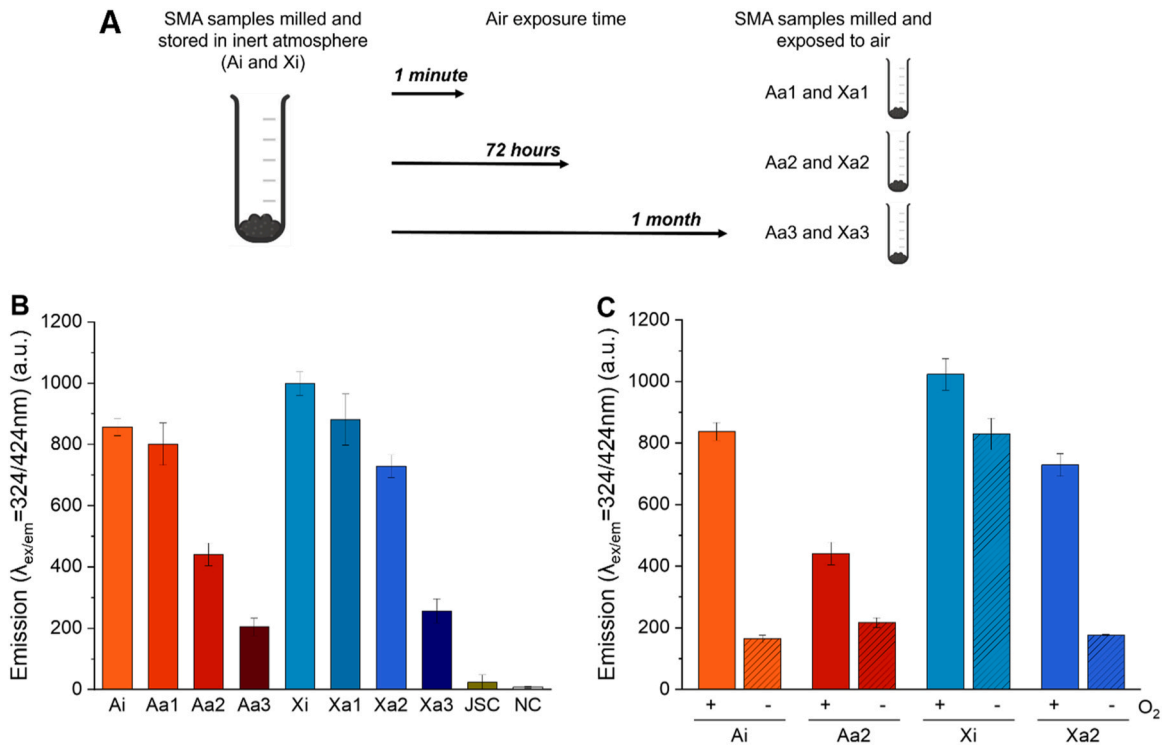

Fig. 5. (**A**) Scheme representing the air exposure times of the SMA samples milled in an inert atmosphere. (**B**) Effect of the atmospheric environment on TA hydroxylation by milled SMA particles. Fluorescence intensity of TA-OH incubated for 48 h with milled SMA particles (5 mg/ml) stored in the inert atmosphere (Ai and Xi) or exposed to air for 1 min (Aa1 and Xa1), 72 h (Aa2 and Xa2) and 1 month (Aa3 and Xa3). JSC refers to JSC-1A-1v and is used as positive reference material. NC refers to negative control (*i.e.*, media without dust). (**C**) Effect of an oxygen-deprived atmosphere on TA hydroxylation by milled SMA particles preserved in an inert atmosphere (Ai and Xi) or exposed for 72 h to air (Aa2 and Xa2). The mean ± standard deviation (SD) of three independent experiments is reported.

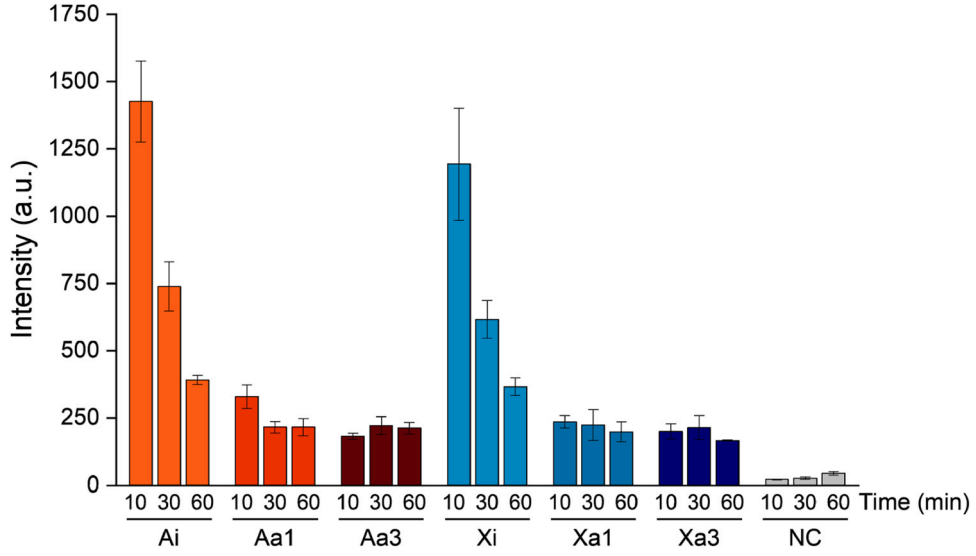

Fig. 6. Kinetics of Fenton-like $^{\bullet}$OH radical generation in solution from milled SMA particles stored in the inert atmosphere (Ai and Xi) and exposed to air for 1 minute (Aa1 and Xa1) and 1 month (Aa3 and Xa3). Milled SMA particles (16 mg/ml) were incubated in PB (10 mM, pH 7.4), H_2O_2, and DMPO as spin trapping agent. EPR spectra were recorded at 10, 30 and 60 min and the signal double integrated to obtain radical amount. NC refers to negative control (i.e., media without dust). The mean ± SD of two independent experiments is reported.

stable over time, if compared to the negative control.

Overall, these results showed the relevance of the atmospheric environment to the oxidant activity of SMA samples. Both type A and type X SMA showed similar trends of activity, albeit Xi appeared less affected by O_2 for TA hydroxylation. We thus hypothesized that the atmospheric environment could affect the state of redox-active iron at the particle surface that may or may not catalyze the Fenton reaction. In fact, only reduced Fe can catalyze $^{\bullet}$OH radical formation, while Fe^{3+} ions are not active. To confirm this hypothesis, bioavailable iron, i.e., the Fe atoms that can be leached in ionic form from the SMA surface, was assessed.

3.3. The atmospheric environment affects the bioavailable iron state on SMA particle surface

To gain information on the iron speciation at the uppermost atomic layer of SMA, we quantitatively evaluated the release in aqueous solution of total ($Fe^0 + Fe^{2+} + Fe^{3+}$) and reduced ($Fe^0 + Fe^{2+}$) iron atoms over time. The kinetics of the release of total or reduced iron species from milled SMA samples were evaluated with the chelator ferrozine/ascorbic acid or ferrozine alone, respectively. The release of total or reduced iron in a short time (over 60 min) is reported in Fig. 7A and B, respectively. Milled SMA samples stored in inert atmosphere (Ai and Xi) induced a rapid release of both total (Fig. 7A) and reduced (Fig. 7B) iron that attained the maximum (ca. 11–16 ng/ml) after 5 min of incubation. Being the kinetics of total and reduced iron release very similar, this indicates that most of the bioavailable iron in SMA stored in inert atmosphere occurs as reduced iron, which includes both leachable Fe^{2+} and Fe^0 that is oxidized by molecular oxygen dissolved in solution. Milled SMA samples exposed to air (1 month, Aa3 and Xa3) induced a slightly slower release of total iron compared to samples stored in inert atmosphere (Fig. 7A), attaining the maximum after ca. 30 min. Notably, for Aa3 and Xa3, the release of reduced iron over 60 min was very low (Fig. 7B). This suggests that in the short time (60 min) almost all the released iron from these samples is in the form of oxidized iron (Fe^{3+}). In 60 min, the kinetic trends of both total and reduced iron release were comparable between the two SMA samples, when stored in the same conditions (*i.e.*, Ai *vs* Xi, and Aa3 *vs* Xa3).

At longer incubation times (up to 120 h) (Fig. 7C and D), the total iron release trends for samples in inert atmosphere or exposed to air became almost superimposable (Fig. 7C), but the kinetics of reduced iron release differed significantly for Aa3 and Xa3 compared to their counterparts in the inert atmosphere (Fig. 7D). For Xa3, the reduced iron level increased to match the total iron (ca. 14 ng/mg) after 24 h, whereas, for Aa3, the reduced iron level remained low throughout the incubation period (max ca. 7 ng/mg at 120 h).

3.4. Milled SMA particles do not induce membranolysis

Cell membrane damage, a possible toxic outcome of LD-generated ROS, was evaluated on RBCs incubated with increasing doses of milled SMA particles stored in inert atmosphere (Ai and Xi) or exposed to air (Aa and Xa). RBCs are largely used as an *in vitro* proxy of toxicity mechanisms associated with cell membrane damage and particle-induced inflammatory response by particulates, and to evaluate the biocompatibility of materials in general [42,43]. Because RBCs are non-internalizing cells, the interaction with SMA particles is confined to the outer lipid bilayer of the RBC cytoplasmatic membrane, which acts as a probe of membranolytic sites on particle surface [45,57]. The quartz Min-U-Sil 5 was used as a positive reference material because of its well-known membranolytic and pathogenic activity [49,53]. All SMA samples, independently from the atmospheric environment to which they were exposed, did not cause RBC lysis (i.e., hemolysis) at any dose investigated (Fig. 8). Possible interference due to hemoglobin adsorption by SMA particles was preventively checked (Supporting Material, Fig. S5), and none of the SMA samples significantly adsorbed

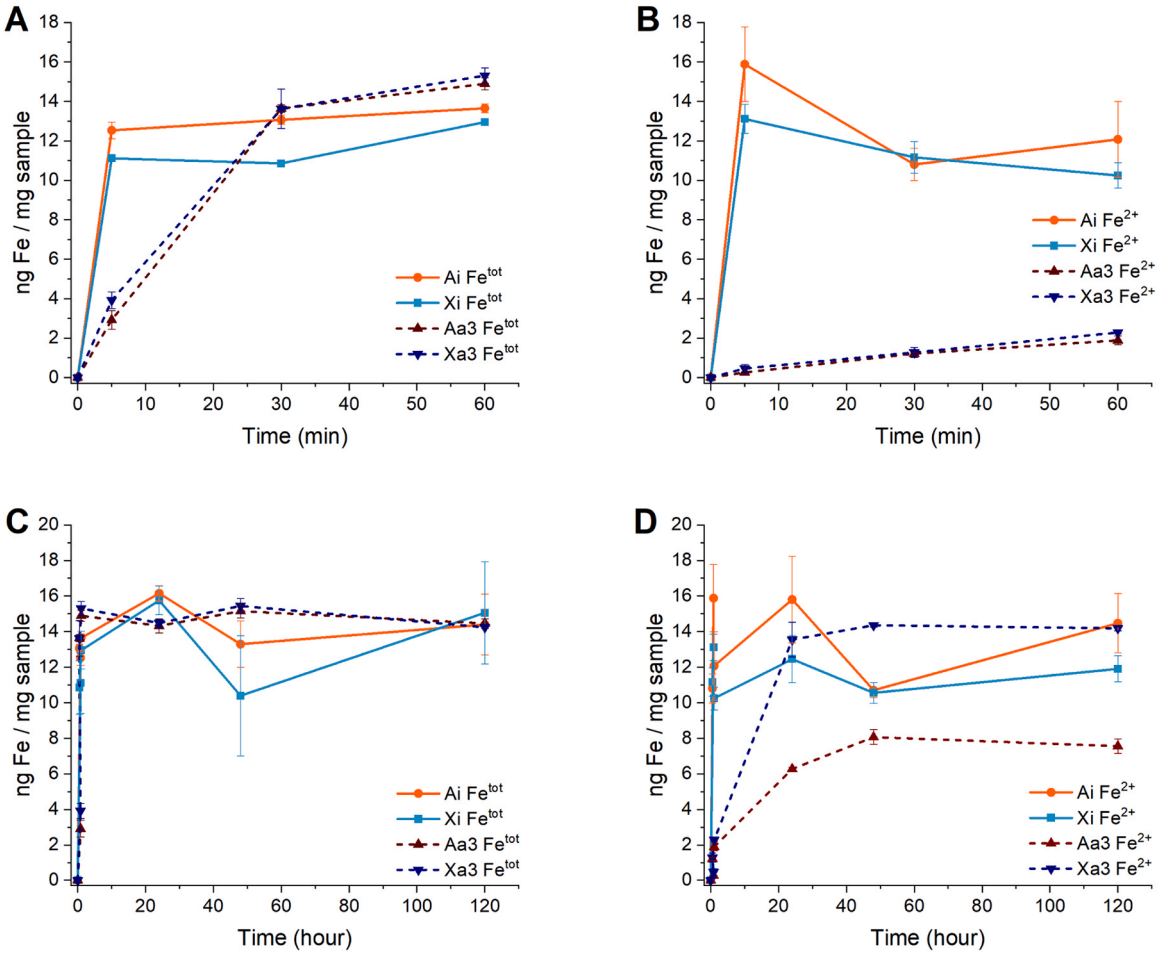

Fig. 7. Short (up to 60 min) (**A, B**) and long-time (up to 120 h) (**C, D**) kinetics of bioavailable iron, (**A, C**) total iron and (**B, D**) reduced Fe^{2+}, in aqueous solution from milled SMA particles stored in inert atmosphere (Ai and Xi) or exposed to air (for 1 month, Aa3 and Xa3). The mean ± SD of two independent experiments (two replicates for each experiment) is reported.

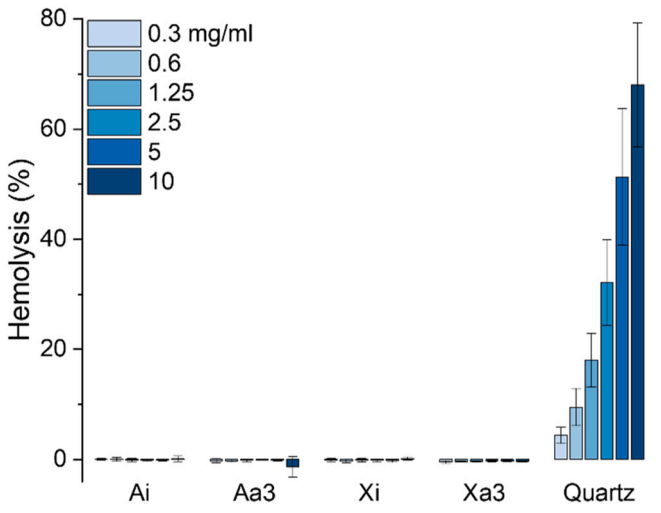

Fig. 8. Membranolytic activity (% hemolysis) of the milled SMA particles. Increasing concentrations (i.e., 0.3, 0.6, 1.2, 2.5, 5 and 10 mg/ml) of milled SMA particles stored in inert atmosphere (Ai and Xi) or exposed to air (Aa and Xa) were incubated for 30 min with purified sheep RBCs. Quartz was used as a positive reference particle. Values reflect the fraction of the total hemoglobin content released and are reported as mean ± SD of three independent experiments.

hemoglobin.

4. Discussion

The toxicity of lunar dust (LD) has been identified as a significant challenge to ensuring human health and enabling sustained activities on the Moon [6,13]. Due to the limited availability of real LD samples, most research in this field depends on the use of lunar dust simulants (LDS) [29]. Two recently synthesized LDS, i.e., SMA A and X [34], containing nanophase iron (np-Fe^0), were here used to investigate the effect of the atmospheric environment on their surface reactivity and capacity to induce oxidative stress. The presence of np-Fe^0 in a glassy silicate matrix is indeed a peculiar feature of real LD [9–11], possibly involved in its cytotoxic and inflammatory effect [7,24,25]. In our hypothesis, the oxygen- and water vapor-free lunar environment may enhance the reactivity of these iron centers that are formed and exposed on LD surface during micro-meteorites bombardment. The lunar environment was recreated at lab scale by milling the two pristine SMA samples (Xp and Ap) in an argon-sealed jar. The milled SMA particles were stored in argon (Ai and Xi, initial state) or exposed at different time points to air (Aa and Xa), to simulate the surface passivation that might occur to LD upon admittance of the dust to the life-supporting atmosphere of the interlock chamber.

The milling procedure effectively reduced the size of pristine SMA particles down to the size of real LD (95 % < 10 μm) (Figs. 1 and 2), as recently confirmed by the Chang'e 5 mission returned samples [58]. The larger particle size fraction was reduced toward the respirable size range, particularly for Xp, which initially exhibited a larger size than Ap (Fig. 2B). The very fine nature of LD accounts for its relevant impact on the human respiratory apparatus, as most of the particles are virtually able to penetrate the unciliated airways [54,59].

Furthermore, milling increased the amount of iron clusters exposed on the surface of the SMA glassy matrix, as confirmed by XRD and XPS data (Figs. 3 and 4, Tables 1 and 2). This agrees with findings on isolated respirable-sized real LD, where the concentration of np-Fe^0 domains increased as particle size decreased to 2 μm [60]. SEM imaging of the pristine SMA particle surface revealed well-defined cubic structures of *ca.* 50–150 nm (Fig. 1). Due to their higher brightness in BSE imaging compared to the matrix, these cubic structures were consistent with the occurrence of np-Fe^0. Very similar observations have been made on a real LD, where np-Fe^0 spherules appeared as bright areas in BSE images [60]. SEM/BSE imaging (Fig. 1) and XRD data (Fig. 3 and Table 1) showed that milling altered the surface regularity of the cubic structures and reduced the size of np-Fe^0 crystallites, while preserving their crystallinity.

The impact of the atmospheric environment on the ability of SMA particles to induce oxidative stress, as demonstrated by TA hydroxylation (Fig. 5), revealed that SMA particles milled and stored in inert atmosphere (Xi and Ai) strongly induced the generation of $^{\bullet}OH$ in aqueous solution (Fig. 5B), without the need for external catalysts such as UV irradiation or hydrogen peroxide, which are typically required to promote Fenton reaction [61,62]. This intrinsic reactivity signals the availability at SMA surface of np-Fe^0 with high specific surface area and electronic properties that may facilitate rapid electron transfer processes. The hydroxylation of TA was markedly decreased, though not completely inhibited, when the reaction was carried out in an oxygen-deprived environment (Fig. 5 C). This highlights the essential role of oxygen in the hydroxylation reaction of TA and confirms the Fe^0-driven mechanism that requires molecular O_2. The reduction of O_2 by Fe^0 (Eq. 2) [35,36] or by Fe^0 corrosion products (Eqs. 4–6) [37–40] leads to the formation of Fenton reactants, which in turn produce $^{\bullet}OH$ species through the Fenton reaction (Eq. 1).

The $^{\bullet}OH$ can promote an addition on TA ring to form the hydroxylated fluorescent 2-hydroxy TA product. The chemistry of heterogenous Fenton systems, in which soluble Fe^{2+} is replaced by Fe-containing solids, is of considerable interest for environmental remediation processes, offering the possibility to operate at near neutral pH and to recycle the iron promoter [63]. Indeed, in nano zero-valent iron systems, Fe^{3+} is rapidly recycled back to Fe^{2+} at the surface of the Fe^0 nanoparticulate [36]:

$$2Fe^{3+} + Fe^0 \rightarrow 3Fe^{2+} \quad (8)$$

This peculiarity may explain the high reactivity of our SMA dusts, even after long incubation time, as the presence of np-Fe^0 can act as an electron-donor reservoir, slowly releasing dissolved Fe^{2+} [63,64]. Milling SMA powder might also produce an increase in activity for the Fenton-like reaction, as reported for Fe^0/Fe_3O_4 composites [63,64]. It is noteworthy that a residual hydroxylation of TA persisted in an oxygen-free environment, particularly for Xi. A limited number of studies have tried to demonstrate how nano zero-valent iron can reduce organic molecules under oxygen-deprived conditions, even at neutral pH, through direct or indirect mechanisms [65]. However, discussing our present results in the light of those mechanisms would be rather speculative due to the complexity and inherent differences between the investigated systems.

When milled SMA dust was exposed to air (Aa and Xa), TA hydroxylation decreased in a time-dependent manner (Fig. 5B). The impact of air exposure was evident as early as 1 minute, with a significant reduction observed after 72 hours and a more pronounced decline after 1 month. This decrease could be due to passivation of surface np-Fe^0 by atmospheric O_2 forming Fe oxides [66]. Despite this decrease in TA hydroxylation, the oxidant activity of SMA dust remained higher than that of JSC-1A-vf, even after 1 month of air exposure. This finding highlights the critical role of np-Fe^0 clusters in driving the generation of $^{\bullet}OH$ radicals, as JSC-1A-vf lacks the np-Fe^0 inclusions [33,34], and underscore the relevance of using high fidelity LDS to accurately evaluate the potential health hazard associated with LD.

Release of Fenton-like $^{\bullet}OH$ radicals, as assessed by EPR/spin trap experiments using H_2O_2 (Fig. 6), consistently showed a strong release from samples preserved in inert conditions (Xi and Ai) and a strong decrease (Aa and Xa) when SMA samples were exposed to air. The kinetic of Fenton-like $^{\bullet}OH$ radical generation of Xi and Ai showed a dramatic decrease over 1 h. During this time, the samples were maintained in contact with the reagents, and a rapid consumption of Fe^{2+},

associated with passivation of np-Fe^0 surface by oxidized iron compounds, i.e., oxides/hydroxides formed in the presence of O_2 [66], and a quenching effect of the DMPO-OH radical by Fe^{2+} [67] might have occurred. The Fenton-radical activity of milled samples was reduced almost instantly (1 min, Aa1 and Xa1) after contact with the oxidant environment. This might not seem entirely consistent with TA hydroxylation results, where radical activity decreased only slightly when samples were exposed to air for 1 minute. However, it should be considered that the two tests were conducted with different sample incubation times and in a different reaction environment. Specifically, while the spin trap approach measures the $^{\bullet}OH$ radicals formed in the initial minutes of sample contact with an oxidative regent ($+H_2O_2$), the TA test quantifies radicals that formed over a 48-h long incubation time, in a solution where the only reducible species is dissolved molecular O_2, for a pH > 4. Moreover, the highest sensitivity of the TA test in the micro molar range (Supporting Material; Fig. S2), as compared to the detectable spin adduct DMPO-OH in the millimolar range [68], may support further the differentiated and complementarity of the two reactivity measures. As observed for TA hydroxylation, despite the significant decrease, the Fenton-like $^{\bullet}OH$ radical generation induced by samples exposed to air remained intense and stable over time, even after 1 month (Aa3 and Xa3) (Fig. 6). As mentioned above, this may be ascribed to np-Fe^0, which can act as an electron-donor reservoir, gradually releasing dissolved Fe^{2+} [63,64].

The determination of bioavailable iron (Fig. 7) supported this hypothesis. Variations in radical activity could be attributed to the presence of iron in different oxidation states, whose speciation depends on SMA type and the atmospheric environment to which the particles were exposed. SMA milled in inert atmosphere only released Fe^{2+} (Fig. 7A-D), either from leaching of oxidized np-Fe^0 or Fe^{2+} at the particle surface. The release of iron ions from the air-exposed samples was initially very slow and occurred mostly as Fe^{3+}(Fig. 7A and B), which is not active in Fenton reaction. After 24 h, the release of Fe^{2+} by Xa3 paralleled the total iron. Fe^{2+} was gradually released (ca. 24 h) also from Aa3, albeit Fe^{2+} never attained the total iron level (Fig. 7C and D), indicating that even at long incubation time, a fraction of iron is still Fe^{3+}. This difference between Xa3- and Aa3-induced Fe^{2+} release (Fig. 7C and D) should explain the observed differences in TA hydroxylation from X and A measured after 48 h of incubation (Fig. 5B). The different cage structures of the two starting zeolites could have determined distinct mechanisms for the release of Fe^{2+} during long incubation times in aqueous suspension, with X showing more Fe^{2+} and a higher radical activity compared to A, even when air exposed (Fig. 5B). This might also explain why X is less affected by O_2 for TA hydroxylation (Fig. 5 C), having intrinsically a higher reducing capacity (higher Fe^{2+} release). The analogous release trend of Fe^{2+} by Aa3 and Xa3 in the very short timing (< 1 h) (Fig. 7A and B) should explain the similar release of Fenton-like $^{\bullet}OH$ radicals from Aa and Xa (Fig. 6).

Despite the strong capacity of milled SMA particles to induce oxidative stress, none of these materials was able to cause RBC membrane damage, contrary to other particulates, such as highly toxic respirable crystalline silica dust [45,53]. This data mechanistically confirmed the lack of relationship between radical release and membranolysis induced by particles [53] or 2D materials [42], suggesting that possible pathway of LD toxicity may mostly reside on their potential to induce cellular oxidative stress.

5. Conclusions

We provided a high-fidelity lunar dust simulant featuring particles in the respirable size and freshly exposed nanophase iron (np-Fe^0). The presence of np-Fe^0 within the samples, along with their ability to form Fe^{2+} and function as heterogenous Fenton system, appeared to be the primary mechanism driving hydroxyl radical release in a biological mimicking solution, with the crucial contribution of dissolved O_2. This effect was notably higher in samples stored in an inert environment, which prevented iron oxidation. Oxidative ageing led to a time-dependent decrease in the ability of the studied dust simulant to generate hydroxyl radicals, because of surface passivation induced by the oxidative atmosphere. In support of these observations, most existing lunar simulants, including JSC-1A, do not contain np-Fe^0 and showed a much lower release of radicals in solution. Further studies may aim to assess the effect of the atmospheric environment on LD cellular oxidative stress and toxicity mechanism.

Environmental implications

Lunar dust (LD), composed of fine particles on the Moon's surface akin to Earth's mineral dust, poses significant health risk to astronauts. Its ability to infiltrate the respiratory system and cause damage stems from its complex origin and specifically from the peculiar occurrence of nanophase metallic iron (np-Fe^0) embedded in a glassy silicate layer. However, the toxic action of LD remains poorly understood due to the scarce availability of returned samples and the complexity of handling the dust in its pristine state. In this study, we developed a novel high-fidelity lunar dust simulant doped with np-Fe^0 to explore its surface biochemical reactivity. By investigating oxidative stress mechanisms and oxidative ageing in a life-supporting atmosphere, we identified fundamental mechanisms of LD chemical reactivity and new potential pathways for its toxic effects. Our results have significant environmental implications, offering essential guidance for protecting astronauts' health during lunar missions and advancing sustainable practices for human space exploration.

CRediT authorship contribution statement

Pavan Cristina: Writing – review & editing, Writing – original draft, Methodology, Investigation, Data curation, Conceptualization. **Pansini Michele:** Writing – review & editing, Supervision, Methodology. **Tomatis Maura:** Writing – original draft, Methodology, Investigation, Data curation. **Turci Francesco:** Writing – review & editing, Writing – original draft, Supervision, Methodology, Funding acquisition, Conceptualization. **Esposito Serena:** Writing – review & editing, Supervision, Funding acquisition, Conceptualization. **Castellino Micaela:** Writing – original draft, Methodology, Investigation. **Tammaro Olimpia:** Writing – original draft, Methodology, Investigation, Data curation. **Petriglieri Jasmine Rita:** Writing – original draft, Methodology, Investigation, Data curation. **Marocco Antonello:** Methodology, Investigation. **Bianco Piero:** Writing – original draft, Investigation, Formal analysis, Data curation.

Declaration of Competing Interest

The authors declare that they have no known competing financial interests or personal relationships that could have appeared to influence the work reported in this paper.

Acknowledgements

The authors thank Dr. Maria Carmen Valsania for the FE-SEM micrographs (Department of Chemistry, University of Turin). CP and FT acknowledge support from Project CH4.0 under the MUR Program "Dipartimenti di Eccellenza 2023–2027" (CUP: D13C22003520001).

Appendix A. Supporting information

Supplementary data associated with this article can be found in the online version at doi:10.1016/j.jhazmat.2025.138096.

Data availability

Data will be made available on request.

References

[1] Evans, M.E., Graham, L.D., 2020. A flexible lunar architecture for exploration (FLARE) supporting NASA's artemis program. Acta Astronaut 177, 351–372. https://doi.org/10.1016/j.actaastro.2020.07.032.

[2] Li, C., Wang, C., Wei, Y., Lin, Y., 2019. China's present and future lunar exploration program. Science 365, 238–239. https://doi.org/10.1126/science.aax9908.

[3] Ding, J., Xu, Y., Tan, J., Zhang, H., Xiong, X., Mei, C., et al., 2024. How to make lunar soil suitable for cultivation? – A review. Sci Total Environ 948, 174603. https://doi.org/10.1016/j.scitotenv.2024.174603.

[4] Pickrell, J., 2022. These six countries are about to go to the Moon — here's why. Nature 605, 208–211. https://doi.org/10.1038/d41586-022-01252-7.

[5] Cui, X., Song, W., Xue, Y., Jing, H., Lei, M., Ma, H., et al., 2024. Numerical analysis of micro lunar dust deposition in the human nasal airway. J Hazard Mater 461, 132682. https://doi.org/10.1016/j.jhazmat.2023.132682.

[6] Corazzari, I., Durante, M., Fubini, B., Gerde, P., Karlsson, L., Linnarsson, D., et al., 2021. History and future perspective for the evaluation of the toxicity of celestial dust. In: Levine, J.S. (Ed.), The Impact of Lunar Dust on Human Exploration. Cambridge Scholars Publishing, Newcastle upon Tyne, pp. 146–189.

[7] Linnarsson, D., Carpenter, J., Fubini, B., Gerde, P., Karlsson, L.L., Loftus, D.J., et al., 2012. Toxicity of lunar dust. Planet Space Sci 74, 57–71. https://doi.org/10.1016/j.pss.2012.05.023.

[8] Park, J., Liu, Y., Kenneth, D.K., Lawrence, A.T., 2008. Characterization of lunar lust for toxicological studies. I: Particle size distribution. J Aerosp Eng 21, 266–271. https://doi.org/10.1061/(ASCE)0893-1321(2008)21:4(266).

[9] Taylor, L.A., Pieters, C.M., Keller, L.P., Morris, R.V., McKay, D.S., 2001. Lunar mare soils: space weathering and the major effects of surface-correlated nanophase Fe. J Geophys Res: Planets 106, 27985–27999. https://doi.org/10.1029/2000JE001402.

[10] Li, C., Guo, Z., Li, Y., Tai, K., Wei, K., Li, X., et al., 2022. Impact-driven disproportionation origin of nanophase iron particles in Chang'e-5 lunar soil sample. Nat Astron 6, 1156–1162. https://doi.org/10.1038/s41550-022-01763-3.

[11] Sorokin, E.M., 2023. Reduced iron in the regolith of the Moon: Review. In: Kolotov, V.P., Bezaeva, N.S. (Eds.), Advances in Geochemistry, Analytical Chemistry, and Planetary Sciences: 75th Anniversary of the Vernadsky Institute of the Russian Academy of Sciences. Springer International Publishing, Cham, pp. 425–440. https://doi.org/10.1007/978-3-031-09883-3_24.

[12] S.A. Wagner, 2006. The Apollo experience lessons learned for constellation lunar dust management. National Aeronautics and Space Administration: NASA/TP-2006-213726.

[13] Miranda, S., Marchal, S., Cumps, L., Dierckx, J., Krüger, M., Grimm, D., et al., 2023. A dusty road for astronauts. Biomedicines 11, 1921. https://doi.org/10.3390/biomedicines11071921.

[14] Khan-Mayberry, N., 2008. The lunar environment: Determining the health effects of exposure to moon dusts. Acta Astronaut 63, 1006–1014. https://doi.org/10.1016/j.actaastro.2008.03.015.

[15] Pohlen, M., Carroll, D., Prisk, G.K., Sawyer, A.J., 2022. Overview of lunar dust toxicity risk. npj Microgravity 8, 55. https://doi.org/10.1038/s41526-022-00244-1.

[16] Lam, C., Scully, R.R., Zhang, Y., Renne, R.A., Hunter, R.L., McCluskey, R.A., et al., 2013. Toxicity of lunar dust assessed in inhalation-exposed rats. Inhal Toxicol 25, 661–678. https://doi.org/10.3109/08958378.2013.833660.

[17] Sun, Y., Liu, J., Zhang, X., Li, X., Zhou, B., Lv, Z., 2019. Mechanisms involved in inflammatory pulmonary fibrosis induced by lunar dust simulant in rats. Environ Toxicol 34, 131–140. https://doi.org/10.1002/tox.22665.

[18] Li, M., Thompson, K.K., Nissen, J.C., Hendrix, D., Hurowitz, J.A., Tsirka, S.E., 2019. Lunar soil simulants alter macrophage survival and function. J Appl Toxicol 39, 1413–1423. https://doi.org/10.1002/jat.3827.

[19] Latch, J.N., Hamilton, R.F., Holian, A., James, J.T., Lam, C., 2008. Toxicity of lunar and martian dust simulants to alveolar macrophages isolated from human volunteers. Inhal Toxicol 20, 157–165. https://doi.org/10.1080/08958370701821219.

[20] Wang, J., Lei, M., Xue, Y., Tan, Q., He, X., Guan, J., et al., 2024. Assessment of toxicity changes induced by exposure of human cells to lunar dust simulant. Sci Rep 14, 24781. https://doi.org/10.1038/s41598-024-69259-w.

[21] Kaur, J., Rickman, D., Schoonen, M.A., 2016. Reactive Oxygen Species (ROS) generation by lunar simulants. Acta Astronaut 122, 196–208. https://doi.org/10.1016/j.actaastro.2016.02.002.

[22] Hendrix, D.A., Catalano, T., Nekvasil, H., Glotch, T.D., Legett, C., Iv, et al., 2024. The reactivity of experimentally reduced lunar regolith simulants: Health implications for future crewed missions to the lunar surface. Meteorit Planet Sci 59, 2487–2504. https://doi.org/10.1111/maps.14228.

[23] Hurowitz, J.A., Tosca, N.J., McLennan, S.M., Schoonen, M.A.A., 2007. Production of hydrogen peroxide in Martian and lunar soils. Earth Planet Sci Lett 255, 41–52. https://doi.org/10.1016/j.epsl.2006.12.004.

[24] Wallace, W.T., Phillips, C.J., Jeevarajan, A.S., Chen, B., Taylor, L.A., 2010. Nanophase iron-enhanced chemical reactivity of ground lunar soil. Earth Planet Sci Lett 295, 571–577. https://doi.org/10.1016/j.epsl.2010.04.042.

[25] Chang, J.H.M., Xue, Z., Bauer, J., Wehle, B., Hendrix, D.A., Catalano, T., et al., 2024. Artificial space weathering to mimic solar wind enhances the toxicity of lunar dust simulants in human lung cells. e2023GH000840 GeoHealth 8. https://doi.org/10.1029/2023GH000840.

[26] Wrigglesworth, J.M., Baum, H., 1980. The biochemical functions of iron. In: Jacobs, A., Worwood, M. (Eds.), Iron in Biochemistry and Medicine. Academic Press, London, pp. 29–86.

[27] Kıran, T.R., Otlu, O., Karabulut, A.B., 2023. Oxidative stress and antioxidants in health and disease. J Lab Med 47, 1–11. https://doi.org/10.1515/labmed-2022-0108.

[28] Liu, Y., Taylor, L.A., 2011. Characterization of lunar dust and a synopsis of available lunar simulants. Planet Space Sci 59, 1769–1783. https://doi.org/10.1016/j.pss.2010.11.007.

[29] A. Slabic, J.E. Gruener, R.N. Kovtun, D.L. Rickman, L. Sibille, H.A. Oravec, , 2024. Lunar regolith simulant user's guide: Revision A. National Aeronautics and Space Administration: NASA/TM-20240011783.

[30] Taylor, L.A., Pieters, C.M., Britt, D., 2016. Evaluations of lunar regolith simulants. Planet Space Sci 126, 1–7. https://doi.org/10.1016/j.pss.2016.04.005.

[31] L. Sibille, P. Carpenter, R. Schlagheck, R.A. French, 2006. Lunar regolith simulant materials: Recommendations for standardization, production, and usage. National Aeronautics and Space Administration: NASA/TP-2006-214605.

[32] Caston, R., Luc, K., Hendrix, D., Hurowitz, J.A., Demple, B., 2018. Assessing toxicity and nuclear and mitochondrial DNA damage caused by exposure of mammalian cells to lunar regolith simulants. GeoHealth 2, 139–148. https://doi.org/10.1002/2017GH000125.

[33] Sen, S., Butts, D., Ray, C.S., Thompson, G.B., Morris, R.A., O'Dell, J.S., 2011. Production of high fidelity lunar agglutinate simulant. Adv Space Res 47, 1912–1921. https://doi.org/10.1016/j.asr.2011.02.005.

[34] Freyria, F.S., Marocco, A., Esposito, S., Bonelli, B., Barrera, G., Tiberto, P., et al., 2019. Simulated moon agglutinates obtained from zeolite precursor by means of a low-cost and scalable synthesis method. ACS Earth Space Chem 3, 1884–1895. https://doi.org/10.1021/acsearthspacechem.9b00042.

[35] Keenan, C.R., Sedlak, D.L., 2008. Ligand-enhanced reactive oxidant generation by nanoparticulate zero-valent iron and oxygen. Environ Sci Technol 42, 6936–6941. https://doi.org/10.1021/es801438f.

[36] Ahmed, N., Vione, D., Rivoira, L., Castiglioni, M., Beldean-Galea, M.S., Bruzzoniti, M.C., 2023. Feasibility of a heterogeneous nanoscale zero-valent iron Fenton-like process for the removal of glyphosate from water. Molecules 28, 2214. https://doi.org/10.3390/molecules28052214.

[37] Noubactep, C., 2009. An analysis of the evolution of reactive species in Fe^0/H_2O systems. J Hazard Mater 168, 1626–1631. https://doi.org/10.1016/j.jhazmat.2009.02.143.

[38] Stratmann, M., Müller, J., 1994. The mechanism of the oxygen reduction on rust-covered metal substrates. Corros Sci 36, 327–359. https://doi.org/10.1016/0010-938X(94)90161-9.

[39] Tao, R., Hu, R., Gwenzi, W., Nanseu-Njiki, C.P., Noubactep, C., 2025. Loss of scientific integrity in using metallic iron (Fe^0) for water remediation: Let's agree to disagree. J Hazard Mater Adv 17, 100595. https://doi.org/10.1016/j.hazadv.2025.100595.

[40] Liu, A., Liu, J., Han, J., Zhang, W., 2017. Evolution of nanoscale zero-valent iron (nZVI) in water: Microscopic and spectroscopic evidence on the formation of nano- and micro-structured iron oxides. J Hazard Mater 322, 129–135. https://doi.org/10.1016/j.jhazmat.2015.12.070.

[41] Dunford, H.B., 1987. Free radicals in iron-containing systems. Free Radic Biol Med 3, 405–421. https://doi.org/10.1016/0891-5849(87)90019-0.

[42] Tiwari, K., Blanquer, A., Pavan, C., Tomatis, M., Navas, N.F., Scaglione, F., et al., 2024. Surface modification of $Ti_{40}Cu_{40}Zr_{11}Fe_3Sn_3Ag_3$ amorphous alloy for enhanced biocompatibility in implant applications. J Mater Res Technol 30, 2333–2346. https://doi.org/10.1016/j.jmrt.2024.03.225.

[43] Pavan, C., Santalucia, R., Escolano-Casado, G., Ugliengo, P., Mino, L., Turci, F., 2023. Physico-chemical approaches to investigate surface hydroxyls as determinants of molecular initiating events in oxide particle toxicity. Int J Mol Sci 24, 11482. https://doi.org/10.3390/ijms241411482.

[44] Weidenthaler, C., Zibrowius, B., Schimanke, J., Mao, Y., Mienert, B., Bill, E., et al., 2005. Oxidation behavior of ferrous cations during ion exchange into zeolites under atmospheric conditions. Microporous Mesoporous Mater 84, 302–317. https://doi.org/10.1016/j.micromeso.2005.04.022.

[45] Bellomo, C., Lagostina, V., Pavan, C., Paganini, M.C., Turci, F., 2024. Reaction with water vapor defines surface reconstruction and membranolytic activity of quartz milled in different molecular environments. Small 20, 2308369. https://doi.org/10.1002/smll.202308369.

[46] Hill, E., Mellin, M.J., Deane, B., Liu, Y., Taylor, L.A., 2007. Apollo sample 70051 and high- and low-Ti lunar soil simulants MLS-1A and JSC-1A: Implications for future lunar exploration. J Geophys Res: Planets 112, E02006. https://doi.org/10.1029/2006JE002767.

[47] Ray, C.S., Reis, S.T., Sen, S., O'Dell, J.S., 2010. JSC-1A lunar soil simulant: Characterization, glass formation, and selected glass properties. J Non-Cryst Solids 356, 2369–2374. https://doi.org/10.1016/j.jnoncrysol.2010.04.049.

[48] Wallace, W.T., Taylor, L.A., Liu, Y., Cooper, B.L., McKay, D.S., Chen, B., et al., 2009. Lunar dust and lunar simulant activation and monitoring. Meteorit Planet Sci 44, 961–970. https://doi.org/10.1111/j.1945-5100.2009.tb00781.x.

[49] Pavan, C., Escolano-Casado, G., Bellomo, C., Cananà, S., Tomatis, M., Leinardi, R., et al., 2023. Nearly free silanols drive the interaction of crystalline silica polymorphs with membranes: Implications for mineral toxicity. Front Chem 10, 1092221. https://doi.org/10.3389/fchem.2022.1092221.

[50] Turci, F., Corazzari, I., Alberto, G., Martra, G., Fubini, B., 2015. Free-radical chemistry as a means to evaluate lunar dust health hazard in view of future missions to the Moon. Astrobiology 15, 371–380. https://doi.org/10.1089/ast.2014.1216.

[51] Horwell, C.J., Fenoglio, I., Fubini, B., 2007. Iron-induced hydroxyl radical generation from basaltic volcanic ash. Earth Planet Sci Lett 261, 662–669. https://doi.org/10.1016/j.epsl.2007.07.032.

[52] Leinardi, R., Pochet, A., Uwambayinema, F., Yakoub, Y., Quesniaux, V., Ryffel, B., et al., 2023. Gasdermin D membrane pores orchestrate IL-1α secretion from necrotic macrophages after NFS-rich silica exposure. Arch Toxicol 97, 1001–1015. https://doi.org/10.1007/s00204-023-03463-x.

[53] Pavan, C., Leinardi, R., Benhida, A., Ibouraadaten, S., Yakoub, Y., Brule, S. van den, et al., 2024. Short- and long-term pathologic responses to quartz are induced by nearly free silanols formed during crystal fracturing. Part Fibre Toxicol 21, 52. https://doi.org/10.1186/s12989-024-00611-8.

[54] Cui, X., Song, W., Xue, Y., Guan, H., Zhang, J., He, X., et al., 2023. Numerical investigations of the micro lunar dust particles deposition in the human oral respiratory airway. J Hazard Mater 448, 130886. https://doi.org/10.1016/j.jhazmat.2023.130886.

[55] Pansini, M., Dell'agli, G., Marocco, A., Netti, P.A., Battista, E., Lettera, V., et al., 2017. Preparation and characterization of magnetic and porous metal-ceramic nanocomposites from a zeolite precursor and their application for DNA separation. J Biomed Nanotechnol 13, 337–348. https://doi.org/10.1166/jbn.2017.2345.

[56] Øvrevik, J., Refsnes, M., Låg, M., Holme, J.A., Schwarze, P.E., 2015. Activation of proinflammatory responses in cells of the airway mucosa by particulate Matter: Oxidant- and non-oxidant-mediated triggering mechanisms. Biomolecules 5, 1399–1440. https://doi.org/10.3390/biom5031399.

[57] Pavan, C., Sydor, M.J., Bellomo, C., Leinardi, R., Cananà, S., Kendall, R.L., et al., 2022. Molecular recognition between membrane epitopes and nearly free surface silanols explains silica membranolytic activity. Colloids Surf B: Biointerfaces 217, 112625. https://doi.org/10.1016/j.colsurfb.2022.112625.

[58] Li, C., Hu, H., Yang, M.-F., Pei, Z.-Y., Zhou, Q., Ren, X., et al., 2022. Characteristics of the lunar samples returned by the Chang'E-5 mission. Natl Sci Rev 9, nwab188. https://doi.org/10.1093/nsr/nwab188.

[59] Brown, J.S., Gordon, T., Price, O., Asgharian, B., 2013. Thoracic and respirable particle definitions for human health risk assessment. Part Fibre Toxicol 10, 12. https://doi.org/10.1186/1743-8977-10-12.

[60] McKay, D.S., Cooper, B.L., Taylor, L.A., James, J.T., Thomas-Keprta, K., Pieters, C. M., et al., 2015. Physicochemical properties of respirable-size lunar dust. Acta Astronaut 107, 163–176. https://doi.org/10.1016/j.actaastro.2014.10.032.

[61] Berto, S., De Laurentiis, E., Scapuzzi, C., Chiavazza, E., Corazzari, I., Turci, F., et al., 2018. Phototransformation of l-tryptophan and formation of humic substances in water. Environ Chem Lett 16, 1035–1041. https://doi.org/10.1007/s10311-018-0714-y.

[62] Rigoletto, M., Laurenti, E., Tummino, M.L., 2024. An overview of environmental catalysis mediated by hydrogen peroxide. Catalysts 14, 267. https://doi.org/10.3390/catal14040267.

[63] Costa, R.C.C., Moura, F.C.C., Ardisson, J.D., Fabris, J.D., Lago, R.M., 2008. Highly active heterogeneous Fenton-like systems based on Fe^0/Fe_3O_4 composites prepared by controlled reduction of iron oxides. Appl Catal B: Environ 83, 131–139. https://doi.org/10.1016/j.apcatb.2008.01.039.

[64] Li, H., Qian, L., Liang, C., Zheng, T., Dong, X., Chen, M., 2023. Enhanced Cr(VI) reduction by zero-valent iron and ferroferric oxide wet ball milling: Synergy of electron storage and electron transfer. Chem Eng J 457, 141254. https://doi.org/10.1016/j.cej.2022.141254.

[65] Karim, S., Bae, S., Greenwood, D., Hanna, K., Singhal, N., 2017. Degradation of 17α-ethinylestradiol by nano zero valent iron under different pH and dissolved oxygen levels. Water Res 125, 32–41. https://doi.org/10.1016/j.watres.2017.08.029.

[66] Guan, X., Sun, Y., Qin, H., Li, J., Lo, I.M.C., He, D., et al., 2015. The limitations of applying zero-valent iron technology in contaminants sequestration and the corresponding countermeasures: The development in zero-valent iron technology in the last two decades (1994–2014). Water Res 75, 224–248. https://doi.org/10.1016/j.watres.2015.02.034.

[67] Li, L., Abe, Y., Kanagawa, K., Usui, N., Imai, K., Mashino, T., et al., 2004. Distinguishing the 5,5-dimethyl-1-pyrroline N-oxide (DMPO)-OH radical quenching effect from the hydroxyl radical scavenging effect in the ESR spin-trapping method. Anal Chim Acta 512, 121–124. https://doi.org/10.1016/j.aca.2004.02.020.

[68] Liu, K.J., Miyake, M., Panz, T., Swartz, H., 1999. Evaluation of DEPMPO as a spin trapping agent in biological systems. Free Radic Biol Med 26, 714–721. https://doi.org/10.1016/S0891-5849(98)00251-2.